$X\mathrm{Fe_4Ge_2}$ (X = Y, Lu) and $\mathrm{Mn_3Pt}$: Filling-enforced magnetic topological metals

Di Wang,[1,2] Feng Tang,[1,2] Hoi Chun Po,[3] Ashvin Vishwanath,[4] and Xiangang Wan[1,2,*]

[1]*National Laboratory of Solid State Microstructures and School of Physics, Nanjing University, Nanjing 210093, China*
[2]*Collaborative Innovation Center of Advanced Microstructures, Nanjing University, Nanjing 210093, China*
[3]*Department of Physics, Massachusetts Institute of Technology, Cambridge, Massachusetts 02139, USA*
[4]*Department of Physics, Harvard University, Cambridge, Massachusetts 02138, USA*

(Received 29 October 2019; accepted 26 February 2020; published 13 March 2020)

Magnetism, coupled with nontrivial band topology, can bring about many interesting and exotic phenomena, so that magnetic topological materials have attracted persistent research interest. However, compared with nonmagnetic topological materials (TMs), the magnetic TMs are less studied, since their magnetic structures and topological phase transitions are usually complex and the first-principles predictions are usually sensitive on the effect of Coulomb interaction. In this work we present a comprehensive investigation of $X\mathrm{Fe_4Ge_2}$ (X = Y, Lu) and $\mathrm{Mn_3Pt}$, and find these materials to be filling-enforced magnetic topological metals. Our first-principles calculations show that $X\mathrm{Fe_4Ge_2}$ (X = Y, Lu) host Dirac points near the Fermi level at high symmetry point S. These Dirac points are protected by $P\mathcal{T}$ symmetry (P and $\mathcal{T}$ are inversion and time-reversal transformations, respectively) and a twofold screw rotation symmetry. Moreover, through breaking $P\mathcal{T}$ symmetry, the Dirac points would split into Weyl nodes. $\mathrm{Mn_3Pt}$ is found to host fourfold degenerate band crossings in the whole high symmetry path of A–Z. We also utilize the GGA + U scheme to take into account the effect of Coulomb repulsion and find that the filling-enforced topological properties are naturally insensitive on U.

DOI: 10.1103/PhysRevB.101.115122

I. INTRODUCTION

The topological nature of electronic bands has attracted tremendous attention in condensed matter physics since the birth of the topological insulator [1,2]. During the past decade, a variety of topological materials have been discovered, including topological insulators [1–5], Dirac semimetals [6–10], Weyl semimetals [11–13], node-line semimetals [14–18], topological crystalline insulators [19,20], and various other topological phases [21–27]. It is well known that the nontrivial band topology is usually protected by time-reversal ($\mathcal{T}$) symmetry or other spatial symmetries such as mirror symmetry, glide symmetry, etc. [26]. Furthermore, symmetry and band topology are intertwined with each other, and as a result symmetry information can be used to diagnose the band topology in a highly efficient manner. Nowadays the time-reversal-invariant topological materials (TMs) have been extensively studied in both theories and experiments. Recently, symmetry-based methods for the efficient discovery of topological materials were developed [28–31], and thousands of nonmagnetic TM candidates have been proposed [32–34].

Compared to the time-reversal-invariant topological materials, magnetic topological materials are also expected to show rich exotic phenomena [35], such as axion insulators [36–43], antiferromagnetic topological insulator [40–47], magnetic Dirac semimetal [48–51], and magnetic Weyl semimetals [11,52]. However, the predictions on magnetic TMs are relatively rare and very few of them have been realized in experiments up to now [35]. This limitation is originated from the fact that the topological properties are usually accompanied by significant spin-orbit coupling (SOC), while SOC typically leads to complex magnetic structures which are difficult to characterize experimentally and theoretically. Moreover, unlike nonmagnetic systems, Coulomb interaction is of substantial importance in most magnetic systems, and the Coulomb repulsion is usually incorporated by the parameter U in first-principles calculations. Therefore, the first-principles predictions for magnetic topological materials usually depends on the value of U [11,38,52].

Recently, the filling constraint for a band insulator has been established to discover topological semimetals [53,54]. This method enables the efficient search for filling-enforced topological materials solely on their space group (SG) and the filling electron number. The central logic is that there is a tight bound for fillings of a band insulator in a SG [53]. Once a material crystallizing in this SG owns the number of valence electrons per unit cell out of the tight bound, it cannot be an insulator. Based on the filling-constraint method [53,54], one can readily calculate the filling constraint ν_{BS} for a material according to its SG, where ν represents the filling number of occupied electrons per unit cell. If $\nu \notin \nu_{BS} \cdot \mathbb{Z}$ (here $\mathbb{Z}$ represents any integer), this material has an electron filling incompatible with any band insulator, and it must have symmetry-protected gaplessness near the Fermi energy (unless a further symmetry-breaking or correlated phase is realized). This type of material is referred to as filling-enforced (semi)metals [53,54]. Moreover, the filling-constraint method has been extended to magnetic materials based on their magnetic space group (MSG) symmetries [55]. Note that the filling-constraint method is based on the interplay between electron filling and (magnetic) space group symmetries, and

*Corresponding author: xgwan@nju.edu.cn

therefore it is insensitive to the precise value of U so long as the relevant symmetries are preserved.

In this work, by applying the filling-constraint method [53–55], we find several magnetic topological metals: XFe $_4$Ge$_2$ (X = Y, Lu) and Mn_3Pt. We display detailed analysis for the topological features of XFe$_4$Ge$_2$, where Dirac points are located at S point near the Fermi energy. Moreover, the calculations show that the Dirac points would split into Weyl nodes by a small perturbation. We also perform the first-principles calculations for the high-temperature phase of Mn_3Pt, where the bands along the A–Z path are fourfold degenerate. The results show that the essential properties and our conclusions do not depend on the value of U as we expected.

II. METHOD

The calculations of electronic band structure and density of states have been carried out as implemented in the Vienna *ab initio* simulation package (VASP) [57–59]. The Perdew–Burke–Ernzerhof (PBE) of generalized gradient approximation (GGA) is chosen as the exchange-correlation functional [60]. $6 \times 6 \times 12$ and $16 \times 16 \times 8$ k-point meshes are used for the Brillouin zone (BZ) integral in XFe$_4$Ge$_2$ (X = Y, Lu) and Mn_3Pt system, respectively. The self-consistent calculations are considered to be converged when the difference in the total energy of the crystal does not exceed 0.01 mRy. The effect of spin-orbit coupling (SOC) [61] is considered self-consistently in all the calculations. We also utilize the GGA + U scheme [62] to take into account the effect of Coulomb repulsion in 3d orbital and the value of parameter U is varied between 0 and 4 eV.

III. RESULTS

YFe$_4$Ge$_2$ was previously reported to crystallize in the ZrFe$_4$Ge$_2$ type of structure with the space group $P4_2/mnm$ at room temperature [63]. In this tetragonal structure, YFe$_4$Ge$_2$ has two formula units in the primitive unit cell [63]. In 2001, Schobinger-Papamantellos *et al.* [56] measured the neutron diffraction and magnetic properties of YFe$_4$Ge$_2$, and found a magnetostructural (ferroelastic and antiferromagnetic) transition, where the magnetic transition at $T_N = 43.5$ K is accompanied by a first-order phase transition from tetragonal structure ($P4_2/mnm$) to orthorhombic structure ($Pnnm$). The magnetic structure below T_N is noncollinear antiferromagnetic with the type-III magnetic space group $Pn'n'm'$ (58.399 in the Belov-Neronova-Smirnova (BNS) settings [64]), as shown in Fig. 1. Note that the magnetic moments on two sites related by the inversion symmetry (P) point in opposite directions, thus YFe$_4$Ge$_2$ is invariant under $P\mathcal{T}$ symmetry ($\mathcal{T}$ is the time-reversal transformation). The magnetic moments of Fe ions at two sites are measured to be 0.63 μ_B per Fe ion equally at 1.5 K. Similar to YFe$_4$Ge$_2$, LuFe$_4$Ge$_2$ has the first-order magnetoelastic transition at $T_N = 32$ K from nonmagnetic tetragonal structure to antiferromagnetic orthorhombic structure, while the Fe moment value is 0.45 μ_B [65]. These materials are suggested to be filling-enforced topological materials [55], as we show in the following.

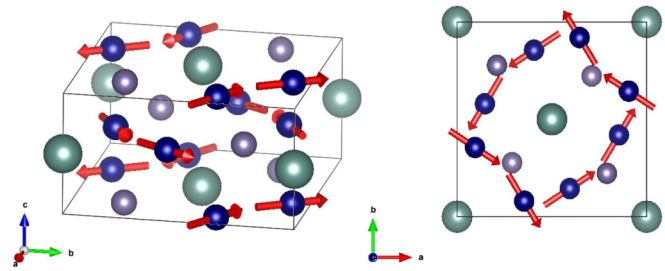

FIG. 1. Crystal structure of YFe$_4$Ge$_2$. The green, blue, and purple balls represent the Y, Fe, and Ge ions, respectively. The arrows denote the ground magnetic order measured by Ref. [56].

Based on the noncollinear antiferromagnetic configuration suggested by neutron diffraction experiment [56] as shown in Fig. 1, we perform the first-principles calculations for YFe$_4$Ge$_2$. The density of states and the band structures are shown in Fig. 2(a) and Figs. 3(a)–3(c), respectively. It should be noted that, due to $P\mathcal{T}$ symmetry, the electronic bands in the whole BZ are doubly degenerate, as shown in Fig. 3. The bands in the energy range from −10.0 to −8.0 eV are mainly contributed by Ge-4s states, while Y bands appear mainly above 3.0 eV. The 3d states of Fe ions are mainly located from −6.0 to 2.0 eV, while Ge-4p states appear mainly between −6.0 and −2.0 eV, implying strong hybridization between Fe and Ge states, as shown in Fig. 2(a). Due to hybridization between Fe and Ge states, the Ge ion has a small calculated magnetic moment (∼0.05 μ_B), but the major magnetic moment is still located at the Fe site. Our calculated magnetic moments of Fe ions at two Fe sites are 1.86 and 1.70 μ_B, which is larger than the experimental value. Though GGA calculations often underestimate the magnetic moments [66], in certain cases the magnetic moments could be overestimated. Similar discrepancy has also been reported in the calculations for other Fe-based intermetallic compounds [67]. For the YFe$_4$Ge$_2$ system, the filling constraint ν_{BS} for its MSG 58.399 is 4 [53–55]. Meanwhile, the number of electrons

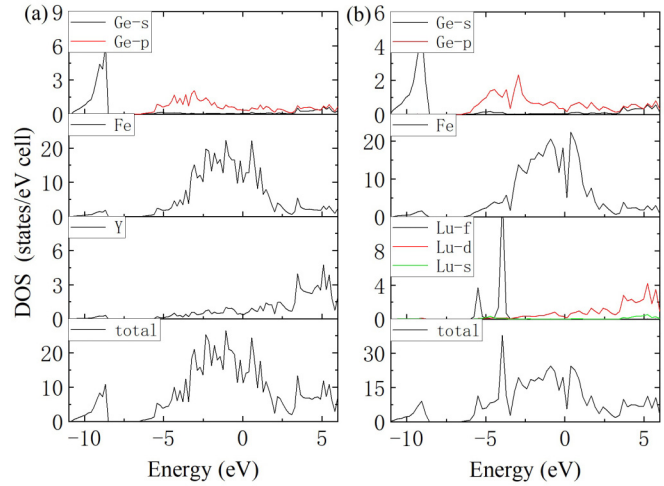

FIG. 2. Partial density of states (PDOS) of YFe$_4$Ge$_2$ (left) and LuFe$_4$Ge$_2$ (right) from GGA calculation with noncollinear antiferromagnetic configuration. The Fermi energy is set to zero.

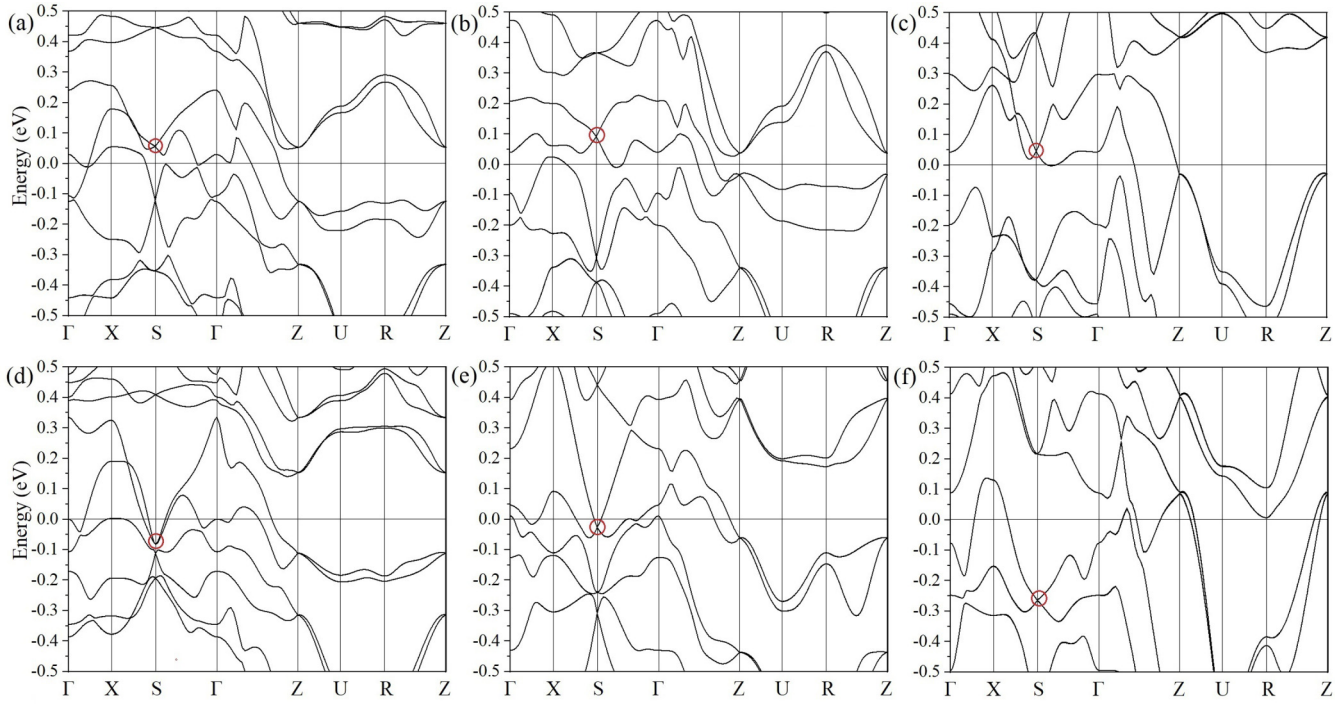

FIG. 3. Band structures of XFe$_4$Ge$_2$ (X = Y, Lu) with experimental magnetic configuration [56]. (a)–(c) Band structures of YFe$_4$Ge$_2$ from GGA, GGA + U (U = 2 eV) and GGA + U (U = 4 eV) calculations, respectively. (d)–(f) Band structures of LuFe$_4$Ge$_2$ from GGA, GGA + U (U = 2 eV) and GGA + U (U = 4 eV) calculations, respectively. The Fermi energy is set to zero. The Dirac points near the Fermi level are marked with red circle.

per unit cell for YFe$_4$Ge$_2$ is to ν = 414, thus $\nu \notin \nu_{BS} \cdot \mathbb{Z}$, indicating that YFe$_4Ge_2$ must be a filling-enforced material. It should be noted that our calculated magnetic moments of Fe ions incorporates all the symmetry restrictions, and the filling-enforced properties predicted in this work are robust as long as the relevant symmetries are preserved.

However, the filling-constraint method does not provide the detailed topological properties. As shown in the symmetry analysis at S point in the next section, only a four-dimensional irreducible representation is allowed, thus all the states at the S point must be grouped into Dirac points. While this conclusion holds for all materials in the same magnetic space group, the filling of YFe$_4$Ge$_2$ implies these Dirac points are naturally close to the Fermi energy. As shown in Fig. 3(a), there is a Dirac point at only 56 meV above the Fermi level at S point, while the Dirac point below the Fermi level is relatively far away (at about −120 meV). We also take into account the effect of Coulomb repulsion in Fe-3d orbital by performing the GGA + U calculations. The value of U around 2 eV is commonly used in the Fe-based intermetallic compound [68,69]. We have varied the value of U from 0 to 4.0 eV (U = 0 eV represents GGA calculation without U), and the calculations show that the position of the Dirac point is kept at the S point with slightly varying energy near the Fermi level, as shown in Figs. 3(a)–3(c). As mentioned above, the filling-constraint method depends only on electron filling and magnetic space group symmetries, thus the filling-enforced topology is not sensitive to the calculation details.

We also perform the first-principles calculations of LuFe$_4$Ge$_2$ whose the band structures and the density of states are shown in Figs. 3(d)—3(f) and Fig. 2(b), respectively. Except for Lu-4f states which are located around −5 eV, the electronic properties of LuFe$_4$Ge$_2$ are very similar to YFe$_4$Ge$_2$, as shown in Figs. 2(b) and 2(a). The filling number of electrons per unit cell is found to be ν = 478, thus $\nu \notin \nu_{BS} \cdot \mathbb{Z}$, also identifying LuFe$_4Ge_2$ as featuring Dirac points pinned at S point near the Fermi level.

As mentioned above, YFe$_4$Ge$_2$ exhibits an antiferromagnetic order with opposite spins related by inversion, and so $P\mathcal{T}$ symmetry is present and the electronic bands are doubly degenerate everywhere. Upon breaking the $P\mathcal{T}$ symmetry, the Dirac cone may split into Weyl nodes [70]. Note that with the $P\mathcal{T}$ symmetry and the twofold rotation $\{2_{001}|0\}$ symmetry coexisting in this system, the z-direction component of Fe magnetic moment m_z should be zero, and the magnetic moments are lying in the xy plane. By a small perturbation such as external field, the magnetic configuration may have a nonzero z-direction component with $P\mathcal{T}$ symmetry broken while $\{2_{001}|0\}$ is preserved, and the Dirac cone may split into Weyl nodes. Accordingly, we perform the GGA calculations with the magnetic state where the magnetic moments have the deflection angle about 2° from the xy plane. As shown in Fig. 4, at S point, all the Dirac points indeed split into Weyl points, while the splitting energies of the upper and lower Dirac points around Fermi level are 6 and 40 meV, respectively. In addition, there is also a symmetry-protected band crossing in the path X-S, as shown in Fig. 4. As discussed in the symmetry analysis below, the hybridization between the red and blue bands in the set of Fig. 4 is forbidden and there is an unavoidable crossing point located at X-S line. Similarly, the first-principles results show that there is also an unavoidable band crossing point along the path Y-S, as shown

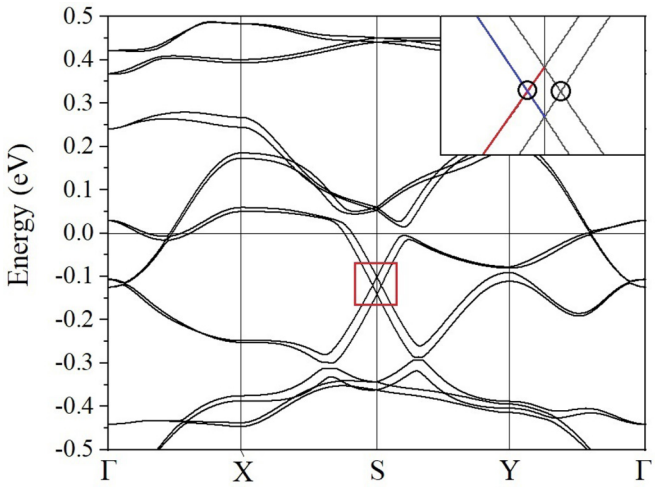

FIG. 4. Band structures of YFe_4Ge_2 from GGA calculation with the magnetic configuration that is slightly deviated from the ground state. The Fermi energy is set to zero. The inset is the detailed structure around S point. The red and blue line represent the eigenstates of $\{2_{010}|1/2, 1/2, 1/2\}$ with the eigenvalues $-ie^{-i\pi k_y}$ and $+ie^{-i\pi k_y}$, respectively. The Weyl points along X-S line and Y-S line are marked with black circle.

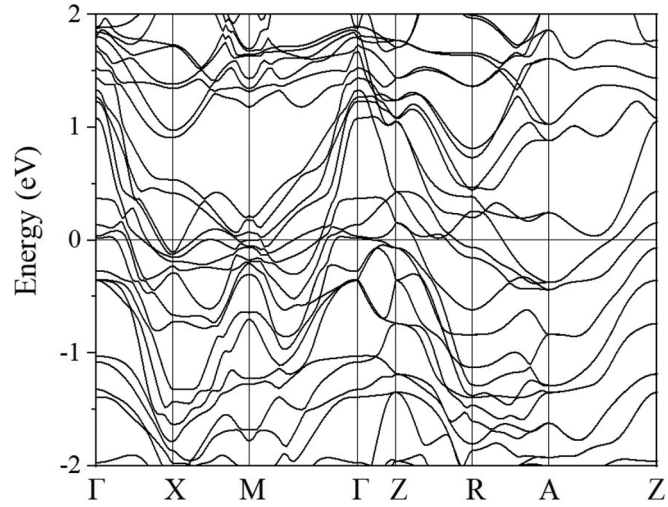

FIG. 5. Band structures of Mn_3Pt with high-temperature collinear antiferromagnetic configuration from GGA calculation. The Fermi energy is set to zero.

in Fig. 4. As shown in Fig. 4, the splitting of Weyl points is very weak due to our small deflection angle, thus the Fermi arc may be short and easy to be buried in bulk states.

We also find the high-temperature phase of a cubic antiferromagnetic intermetallic compound Mn_3Pt as another filling-enforced topological material. Experiment reveals that Mn_3Pt crystallizes in a cubic crystal structure (space group Pm-$3m$) at room temperature and has a long-range antiferromagnetic order with $T_N = 475$ K [71–73]. Neutron diffraction experiments show a first-order magnetic transition in Mn_3Pt system at about 365 K, between a low-temperature noncollinear antiferromagnetic state and a high-temperature collinear antiferromagnetic state [71–73]. The high-temperature phase of Mn_3Pt is collinear antiferromagnetic with the magnetic space group P_c4_2/mcm (132.456), where the Mn atoms in the xy plane couple antiferromagnetically, and the Mn atoms along z direction also have opposite spin orientations. Very recently, Liu *et al.* [74] reported the observation of the anomalous Hall effect in thin films of the low-temperature phase for Mn_3Pt. They also show that the anomalous Hall effect can be turned on and off by applying a small electric field at a temperature around 360 K and the Mn_3Pt is close to the phase transition [74]. Therefore exploring the possible exotic properties of the high-temperature phase for Mn_3Pt is also an interesting problem.

Similarly, we perform the first-principles calculations based on the high-temperature phase of Mn_3Pt and the band structures are shown in Fig. 5. The high-temperature phase of Mn_3Pt also has $P\mathcal{T}$ symmetry like YFe_4Ge_2, thus the electronic band structures are symmetry-protected doubly degenerate in whole BZ. The calculated magnetic moment at the Mn site is 2.9 μ_B per Mn ion, which is in reasonable agreement with the experiment value 3.4 μ_B [71–73]. The Pt-5d states are mainly located from -6.0 to -3.0 eV. The 3d states of Mn ions appear mainly from -3.0 to 2.0 eV. For Mn_3Pt, the filling number of electrons per unit cell is 306 while the ν_{BS} for its MSG (132.456) is also 4, thus $\nu \notin \nu_{BS} \cdot \mathbb{Z}$, indicating that there is a half-occupied fourfold energy level near Fermi energy. As shown in Fig. 5, the bands are fourfold degenerate in the path of A–Z, which is protected by the symmetry operations of magnetic structure, as shown in the detailed symmetry analysis in the next section. We also vary the value of U from 0 to 4.0 eV and find that the fourfold energy level always exists.

IV. SYMMETRY ANALYSIS

In this section we show the detailed symmetry analysis for the Dirac band crossings. We will first focus on the S point in XFe_4Ge_2 (X = Y, Lu), followed by a corresponding discussion for Mn_3Pt. For the S point (1/2, 1/2, 0), eight symmetry operations are generated by three symmetries: the $P\mathcal{T}$ symmetry $\{-1'|0\}$, a twofold screw rotation $\{2_{100}|1/2, 1/2, 1/2\}$, and a twofold rotation $\{2_{001}|0\}$, where the left part represents the rotation and the right part means the lattice translation. Note that -1 above denotes the inversion symmetry and the superscript prime means an additional time-reversal operation $\mathcal{T}$ here. Since $\{2_{100}|1/2, 1/2, 1/2\}^2 = -\{1|1, 0, 0\}$, where the minus sign originates from the spin rotation, the momentum phase factor equals -1 for a Bloch state at the S point. Thus, the eigenvalues for $\{2_{100}|1/2, 1/2, 1/2\}$ is ± 1. We can then choose the eigenstates $\psi^{\pm}_{nS}$ of $\{2_{100}|1/2, 1/2, 1/2\}$ at S point, where the superscript denotes the eigenvalue of $\{2_{100}|1/2, 1/2, 1/2\}$ and n is the band index. Because $[\{-1'|0\}, \{2_{100}|1/2, 1/2, 1/2\}] = 0$ when acting on the Bloch states at S, operation of $\{-1'|0\}$ will preserve the eigenvalue of $\{2_{100}|1/2, 1/2, 1/2\}$ and result in the other state in the Kramers doublet: i.e., $\{-1'|0\}\psi^{+}_{nS}$ is orthogonal to ψ^{+}_{nS} but with the same eigenvalues of $\{2_{100}|1/2, 1/2, 1/2\}$. Besides, it should be noted that $\{2_{100}|1/2, 1/2, 1/2\}\{2_{001}|0\} = -\{2_{001}|0\}\{2_{100}|1/2, 1/2, 1/2\}$, thus $\{2_{001}|0\}\psi^{\pm}_{nS}$ reverses the eigenvalue of $\{2_{100}|1/2, 1/2, 1/2\}$. So the four orthogonal states $\psi^{+}_{nS}, \{-1'|0\}\psi^{+}_{nS}, \{2_{001}|0\}\psi^{+}_{nS}, \{2_{001}|0\}\{-1'|0\}\psi^{+}_{nS}$ are

degenerate, constituting the basis of the four-dimensional irreducible representation. Therefore, in XFe$_4$Ge$_2$ system, the S point (1/2, 1/2, 0) only allows for four-dimensional irreducible representation.

Based on the $k \cdot p$ method, we build the effective Hamiltonian by using the four relevant states as basis vectors, in the order of ψ^+_{nS}, $\{-1'|0\}\psi^+_{nS}$, $\{2_{001}|0\}\psi^+_{nS}$, $\{2_{001}|0\}\{-1'|0\}\psi^+_{nS}$. To the lowest order in $\mathbf{q}$, the Hamiltonian can be written as

$$\begin{bmatrix} q_xC_5 & 0 & \frac{-iq_zC_1-q_yC_2}{\sqrt{2}} & \frac{q_z(iC_3-C_4)}{\sqrt{2}} \\ 0 & q_xC_5 & \frac{q_z(iC_3+C_4)}{\sqrt{2}} & \frac{iq_zC_1-q_yC_2}{\sqrt{2}} \\ \frac{iq_zC_1-q_yC_2}{\sqrt{2}} & \frac{q_z(-iC_3+C_4)}{\sqrt{2}} & -q_xC_5 & 0 \\ \frac{q_z(-iC_3-C_4)}{\sqrt{2}} & \frac{-iq_zC_1-q_yC_2}{\sqrt{2}} & 0 & -q_xC_5 \end{bmatrix}, \quad (1)$$

where $\mathbf{q} = \mathbf{k} - S$, and C_i $(i = 1, 2, \ldots, 5)$ are parameters. The effective Hamiltonian suggests a linear dispersion in the neighborhood of S. It is worth mentioning that there is also only one four-dimensional irreducible representation in Z point (0, 0, 1/2), and the dispersion around Z point is also linear.

When $P\mathcal{T}$ symmetry is broken, there are only four symmetry operations for the S point (1/2, 1/2, 0) generated by $\{2_{100}|1/2, 1/2, 1/2\}$ and $\{2_{001}|0\}$. As mentioned before, for the eigenstates $\psi^{\pm}_{nS}$ of $\{2_{100}|1/2, 1/2, 1/2\}$ at S point, $\{2_{001}|0\}\psi^{\pm}_{nS}$ reverses the eigenvalue of $\{2_{100}|1/2, 1/2, 1/2\}$. So ψ^+_{nS} and $\{2_{001}|0\}\psi^+_{nS}$ own the same energy and they are orthogonal with each other, constituting the basis of the two-dimensional irreducible representation. Therefore all the states at the S point must be grouped pairwise. Meanwhile, for the k point $(1/2, k_y, 0)$ in the path $X(1/2, 0, 0)$-$S(1/2, 1/2, 0)$, only a twofold screw rotation $\{2_{010}|1/2, 1/2, 1/2\}$ is preserved. Note that $\{2_{010}|1/2, 1/2, 1/2\}^2 = -\{1|0, 1, 0\}$, for k point $(1/2, k_y, 0)$, the eigenvalues should be $\pm ie^{-i\pi k_y}$. As shown in Fig. 4, the first-principles results show that two bands along this line belong to the eigenstates of $\{2_{010}|1/2, 1/2, 1/2\}$ with different eigenvalues. Thus the hybridization between these two bands is forbidden and the band crossing is symmetry protected, as shown in Fig. 4. Using these two eigenstates with eigenvalues of $\pm ie^{-i\pi k_y}$ as basis vectors, we also build the effective Hamiltonian of band crossing along X-S based on the $k \cdot p$ method, and the Hamiltonian to the lowest order in $\mathbf{q}$ can be written as

$$\begin{bmatrix} q_yD_6 & q_z(-iD_1 + D_3) + q_x(-iD_2 + D_4) \\ q_z(iD_1 + D_3) + q_x(iD_2 + D_4) & q_yD_5 \end{bmatrix}, \quad (2)$$

where D_i $(i = 1, 2,..., 6)$ are parameters, and $\mathbf{q} = \mathbf{k} - W$ (W is the position of band crossing). The effective Hamiltonian could be expanded to $\mathcal{H}(\mathbf{q}) = \sum_{i=x,y,z} c_iq_iI + \sum_{i,j=x,y,z} v_{ij}q_i\sigma_j$, where I is the identity matrix while σ is the Pauli matrix. Here $v_{ij}(i, j = x, y, z)$ could be written as

$$\begin{bmatrix} D_4 & 0 & D_3 \\ D_2 & 0 & D_1 \\ 0 & \frac{1}{2}(-D_5 + D_6) & 0 \end{bmatrix}, \quad (3)$$

Therefore the Chern number of the band crossing can be quantified by the value $\mathrm{sgn}[\det(v_{ij})] = \mathrm{sgn}[\frac{1}{2}(D_2D_3 - D_1D_4)(-D_5 + D_6)]$ [11]. By fitting the calculated band dispersion, we obtain $\det(v_{ij}) \neq 0$, thus the Chern numbers of the band crossings are suggested to be ± 1. Similarly, for the k point $(k_x, 1/2, 0)$ in the path $Y(0, 1/2, 0)$-$S(1/2, 1/2, 0)$, $\{2_{100}|1/2, 1/2, 1/2\}$ is preserved and the first-principles results show that there is also a Weyl point along the Y-S path.

In Mn_3Pt, similar to the discussion above, we study the symmetry operations of this magnetic structure and find that there is only one four-dimensional irreducible representation along A–Z path in the BZ: For the path of $A(1/2, 1/2, 1/2)$-$Z(0, 0, 1/2)$, eight symmetry operations are generated by three symmetries: the $P\mathcal{T}$ symmetry $\{-1'|0\}$, a twofold screw rotation $\{2_{110}|0, 0, 1/2\}$, and a mirror operation $\{m_{1-10}|0\}$. Since $\{2_{110}|0, 0, 1/2\}^2 = -\{1|0, 0, 0\}$ (the minus sign is coming from the electron spin), the eigenvalues for $\{2_{110}|0, 0, 1/2\}$ is $\pm i$. We can then choose the eigenstates $\psi^{\pm}_{nA-Z}$ of $\{2_{110}|0, 0, 1/2\}$ in A–Z path, where the superscript denotes the eigenvalue of $\pm i$ and n is the band index. Note that $\{-1'|0\}\{2_{110}|0, 0, 1/2\} = -\{2_{110}|0, 0, 1/2\}\{-1'|0\}$, indicating that $\{-1'|0\}\psi^+_{nA-Z}$ is orthogonal to ψ^+_{nA-Z} but with the same eigenvalues of $\{2_{110}|0, 0, 1/2\}$. Besides, it should be noted that $\{2_{110}|0, 0, 1/2\}\{m_{1-10}|0\} = -\{m_{1-10}|0\}\{2_{110}|0, 0, 1/2\}$, thus $\{m_{1-10}|0\}\psi^{\pm}_{nA-Z}$ reverses the eigenvalue of $\{2_{110}|0, 0, 1/2\}$. So ψ^+_{nA-Z}, $\{-1'|0\}\psi^+_{nA-Z}$, $\{m_{1-10}|0\}\psi^+_{nA-Z}$, $\{m_{1-10}|0\}\{-1'|0\}\psi^+_{nA-Z}$ are again orthogonal and degenerate, constituting the basis of the four-dimensional irreducible representation. Therefore, in a Mn_3Pt system, only a four-dimensional irreducible representation is allowed along the $A(1/2, 1/2, 1/2)$-$Z(0, 0, 1/2)$ path.

V. CONCLUSION

In conclusion, by applying the filling constraints, we discover several magnetic topological metals: XFe$_4$Ge$_2$ (X = Y, Lu) and Mn_3Pt. The first-principles calculations show that YFe$_4$Ge$_2$ is a metal with a Dirac cone located at S point near the Fermi level, which is protected by the symmetry operations of magnetic structure. We have varied the value of U from 0 to 4.0 eV, and the results show that Dirac point always exists, since the topological property is filling-enforced and independent on U. When the magnetic moments have a small nonzero z-direction component, the Dirac point would split into Weyl nodes around the S point. We also perform the first-principles calculations based on the high-temperature collinear antiferromagnetic configuration of Mn_3Pt. The

calculation results and symmetry analysis show that it is also a topological material. Even though there are lots of bands around the Fermi level in these materials, we believe that the Dirac points in $X\mathrm{Fe_4Ge_2}$ (X = Y, Lu) can still be detected experimentally [75–77]. Meanwhile, since the Weyl points can be regarded as a magnetic monopole in the momentum space with an important contribution to the Berry curvature, the topological properties of Weyl nodes may also be observed experimentally [78–80]. Note that the first-principles predictions on magnetic topological materials are relatively rare and usually depend on the value of U. Correspondingly, these filling-enforced topological properties are robust and could be better suited for ideally low-consumption device applications, such as spintronics, quantum computation, and many other potential device applications.

ACKNOWLEDGMENTS

D.W., F.T., and X.W. were supported by the NSFC (Grants No. 11834006, No. 11525417, No. 51721001, and No. 11790311), National Key R&D Program of China (Grants No. 2018YFA0305704 and No. 2017YFA0303203), and the excellent programme in Nanjing University. X.W. also acknowledges the support from the Tencent Foundation through the XPLORER PRIZE. A.V. was supported by a Simons Investigator Award and by the Center for Advancement of Topological Semimetals, an Energy Frontier Research Center funded by the US Department of Energy Office of Science, Office of Basic Energy Sciences, through the Ames Laboratory under its Contract No. DE-AC02-07CH11358. H.C.P. was supported by a Pappalardo Fellowship at MIT and a Croucher Foundation Fellowship.

[1] M. Z. Hasan and C. L. Kane, Colloquium: Topological insulators, Rev. Mod. Phys. **82**, 3045 (2010).
[2] X.-L. Qi and S.-C. Zhang, Topological insulators and superconductors, Rev. Mod. Phys. **83**, 1057 (2011).
[3] H. Zhang, C.-X. Liu, X.-L. Qi, X. Dai, Z. Fang, and S.-C. Zhang, Topological insulators in Bi_2Se_3, Bi_2Te_3 and Sb_2Te_3 with a single Dirac cone on the surface, Nat. Phys. **5**, 438 (2009).
[4] Y. Xia, D. Qian, D. Hsieh, L. Wray, A. Pal, H. Lin, A. Bansil, D. Grauer, Y. S. Hor, R. J. Cava, and M. Z. Hasan, Observation of a large-gap topological-insulator class with a single Dirac cone on the surface, Nat. Phys. **5**, 398 (2009).
[5] Y. L. Chen, J. G. Analytis, J.-H. Chu, Z. K. Liu, S.-K. Mo, X.-L. Qi, H. J. Zhang, D. H. Lu, X. Dai, Z. Fang *et al.*, Experimental realization of a three-dimensional topological insulator, Bi_2Te_3, Science **325**, 178 (2009).
[6] S. M. Young, S. Zaheer, J. C. Y. Teo, C. L. Kane, E. J. Mele, and A. M. Rappe, Dirac Semimetal in Three Dimensions, Phys. Rev. Lett. **108**, 140405 (2012).
[7] Z. Wang, Y. Sun, X.-Q. Chen, C. Franchini, G. Xu, H. Weng, X. Dai, and Z. Fang, Dirac semimetal and topological phase transitions in A_3Bi (A = Na, K, Rb), Phys. Rev. B **85**, 195320 (2012).
[8] Z. Wang, H. Weng, Q. Wu, X. Dai, and Z. Fang, Three-dimensional Dirac semimetal and quantum transport in Cd_3As_2, Phys. Rev. B **88**, 125427 (2013).
[9] Q. D. Gibson, L. M. Schoop, L. Muechler, L. S. Xie, M. Hirschberger, N. P. Ong, R. Car, and R. J. Cava, Three-dimensional Dirac semimetals: Design principles and predictions of new materials, Phys. Rev. B **91**, 205128 (2015).
[10] Y. Du, B. Wan, D. Wang, L. Sheng, C.-G. Duan, and X. Wan, Dirac and Weyl Semimetal in $XYBi$ (X = Ba, Eu; Y = Cu, Ag and Au), Sci. Rep. **5**, 14423 (2015).
[11] X. Wan, A. M. Turner, A. Vishwanath, and S. Y. Savrasov, Topological semimetal and Fermi-arc surface states in the electronic structure of pyrochlore iridates, Phys. Rev. B **83**, 205101 (2011).
[12] H. Weng, C. Fang, Z. Fang, B. A. Bernevig, and X. Dai, Weyl Semimetal Phase in Noncentrosymmetric Transition-Metal Monophosphides, Phys. Rev. X **5**, 011029 (2015).
[13] S.-M. Huang, S.-Y. Xu, I. Belopolski, C.-C. Lee, G. Chang, B. Wang, N. Alidoust, G. Bian, M. Neupane, C. Zhang, S. Jia, A. Bansil, H. Lin, and M. Z. Hasan, A Weyl Fermion semimetal with surface Fermi arcs in the transition metal monopnictide TaAs class, Nat. Commun. **6**, 7373 (2015).
[14] A. A. Burkov, M. D. Hook, and L. Balents, Topological nodal semimetals, Phys. Rev. B **84**, 235126 (2011).
[15] H. Weng, Y. Liang, Q. Xu, R. Yu, Z. Fang, X. Dai, and Y. Kawazoe, Topological node-line semimetal in three-dimensional graphene networks, Phys. Rev. B **92**, 045108 (2015).
[16] R. Yu, H. Weng, Z. Fang, X. Dai, and X. Hu, Topological Node-Line Semimetal and Dirac Semimetal State in Antiperovskite Cu_3PdN, Phys. Rev. Lett. **115**, 036807 (2015).
[17] Y. Kim, B. J. Wieder, C. L. Kane, and A. M. Rappe, Dirac Line Nodes in Inversion-Symmetric Crystals, Phys. Rev. Lett. **115**, 036806 (2015).
[18] Y. Du, F. Tang, D. Wang, L. Sheng, E.-j. Kan, C.-G. Duan, S. Y. Savrasov, and X. Wan, CaTe: A new topological node-line and Dirac semimetal, npj Quant. Mater. **2**, 3 (2017).
[19] L. Fu, Topological Crystalline Insulators, Phys. Rev. Lett. **106**, 106802 (2011).
[20] Y. Ando and L. Fu, Topological crystalline insulators and topological superconductors: From concepts to materials, Annu. Rev. Condens. Matter Phys. **6**, 361 (2015).
[21] Z. Wang, A. Alexandradinata, R. J. Cava, and B. A. Bernevig, Hourglass fermions, Nature (London) **532**, 189 (2016).
[22] J. Langbehn, Y. Peng, L. Trifunovic, F. von Oppen, and P. W. Brouwer, Reflection-Symmetric Second-Order Topological Insulators and Superconductors, Phys. Rev. Lett. **119**, 246401 (2017).
[23] W. A. Benalcazar, B. A. Bernevig, and T. L. Hughes, Electric multipole moments, topological multipole moment pumping, and chiral hinge states in crystalline insulators, Phys. Rev. B **96**, 245115 (2017).
[24] F. Schindler, A. M. Cook, M. G. Vergniory, Z. Wang, S. S. Parkin, B. A. Bernevig, and T. Neupert, Higher-order topological insulators, Sci. Adv. **4**, eaat0346 (2018).

[25] Z. Song, Z. Fang, and C. Fang, $(d-2)$-Dimensional Edge States of Rotation Symmetry Protected Topological States, Phys. Rev. Lett. **119**, 246402 (2017).

[26] A. Bansil, H. Lin, and T. Das, Colloquium: Topological band theory, Rev. Mod. Phys. **88**, 021004 (2016).

[27] N. P. Armitage, E. J. Mele, and A. Vishwanath, Weyl and Dirac semimetals in three-dimensional solids, Rev. Mod. Phys. **90**, 015001 (2018).

[28] H. C. Po, A. Vishwanath, and H. Watanabe, Symmetry-based indicators of band topology in the 230 space groups, Nat. Commun. **8**, 50 (2017).

[29] F. Tang, H. C. Po, A. Vishwanath, and X. Wan, Efficient topological materials discovery using symmetry indicators, Nat. Phys. **15**, 470 (2019).

[30] Z. Song, T. Zhang, Z. Fang, and C. Fang, Quantitative mappings between symmetry and topology in solids, Nat. Commun. **9**, 3530 (2018).

[31] B. Bradlyn, L. Elcoro, J. Cano, M. G. Vergniory, Z. Wang, C. Felser, M. I. Aroyo, and B. A. Bernevig, Topological quantum chemistry, Nature (London) **547**, 298 (2017).

[32] T. Zhang, Y. Jiang, Z. Song, H. Huang, Y. He, Z. Fang, H. Weng, and C. Fang, Catalogue of topological electronic materials, Nature (London) **566**, 475 (2019).

[33] M. G. Vergniory, L. Elcoro, C. Felser, B. A. Bernevig, and Z. Wang, The (high quality) topological materials in the world, Nature (London) **566**, 480 (2019).

[34] F. Tang, H. C. Po, A. Vishwanath, and X. Wan, Towards ideal topological materials: Comprehensive database searches using symmetry indicators, Nature (London) **566**, 486 (2019).

[35] Y. Tokura, K. Yasuda, and A. Tsukazaki, Magnetic topological insulators, Nat. Rev. Phys. **1**, 126 (2019).

[36] R. Li, J. Wang, X.-L. Qi, and S.-C. Zhang, Dynamical axion field in topological magnetic insulators, Nat. Phys. **6**, 284 (2010).

[37] A. M. Essin, J. E. Moore, and D. Vanderbilt, Magnetoelectric Polarizability and Axion Electrodynamics in Crystalline Insulators, Phys. Rev. Lett. **102**, 146805 (2009).

[38] X. Wan, A. Vishwanath, and S. Y. Savrasov, Computational Design of Axion Insulators Based on 5*d* Spinel Compounds, Phys. Rev. Lett. **108**, 146601 (2012).

[39] Y. Xu, Z. Song, Z. Wang, H. Weng, and X. Dai, Higher-Order Topology of Axion Insulator $EuIn_2As_2$, Phys. Rev. Lett. **122**, 256402 (2019).

[40] D. Zhang, M. Shi, T. Zhu, D. Xing, H. Zhang, and J. Wang, Topological Axion States in the Magnetic Insulator $MnBi_2Te_4$ with the Quantized Magnetoelectric Effect, Phys. Rev. Lett. **122**, 206401 (2019).

[41] Y. Gong, J. Guo, J. Li, K. Zhu, M. Liao, X. Liu, Q. Zhang, L. Gu, L. Tang, X. Feng *et al.*, Experimental realization of an intrinsic magnetic topological insulator, Chin. Phys. Lett. **36**, 076801 (2019).

[42] J. Li, Y. Li, S. Du, Z. Wang, B.-L. Gu, S.-C. Zhang, K. He, W. Duan, and Y. Xu, Intrinsic magnetic topological insulators in van der Waals layered $MnBi_2Te_4$-family materials, Sci. Adv. **5**, eaaw5685 (2019).

[43] J. Zhang, D. Wang, M. Shi, T. Zhu, H. Zhang, and J. Wang, Dynamical magnetoelectric effect in antiferromagnetic insulator $Mn_2Bi_2Te_5$, arXiv:1906.07891.

[44] R. S. K. Mong, A. M. Essin, and J. E. Moore, Antiferromagnetic topological insulators, Phys. Rev. B **81**, 245209 (2010).

[45] S. Chowdhury, K. F Garrity, and F. Tavazza, Prediction of Weyl semimetal and antiferromagnetic topological insulator phases in Bi_2MnSe_4, npj Comput. Mater. **5**, 33 (2019).

[46] X. Gui, I. Pletikosic, H. Cao, H.-J. Tien, X. Xu, R. Zhong, G. Wang, T.-R. Chang, S. Jia, T. Valla *et al.*, A new magnetic topological quantum material candidate by design, arXiv:1903.03888.

[47] Y. Deng, Y. Yu, M. Z. Shi, J. Wang, X. H. Chen, and Y. Zhang, Magnetic-field-induced quantized anomalous Hall effect in intrinsic magnetic topological insulator $MnBi_2Te_4$, arXiv:1904.11468.

[48] P. Tang, Q. Zhou, G. Xu, and S.-C. Zhang, Dirac fermions in an antiferromagnetic semimetal, Nat. Phys. **12**, 1100 (2016).

[49] G. Hua, S. Nie, Z. Song, R. Yu, G. Xu, and K. Yao, Dirac semimetal in type-IV magnetic space groups, Phys. Rev. B **98**, 201116(R) (2018).

[50] L. Šmejkal, J. Železný, J. Sinova, and T. Jungwirth, Electric Control of Dirac Quasiparticles by Spin-Orbit Torque in an Antiferromagnet, Phys. Rev. Lett. **118**, 106402 (2017).

[51] S. M. Young and B. J. Wieder, Filling-Enforced Magnetic Dirac Semimetals in Two Dimensions, Phys. Rev. Lett. **118**, 186401 (2017).

[52] G. Xu, H. Weng, Z. Wang, X. Dai, and Z. Fang, Chern Semimetal and the Quantized Anomalous Hall Effect in $HgCr_2Se_4$, Phys. Rev. Lett. **107**, 186806 (2011).

[53] H. Watanabe, H. C. Po, M. P. Zaletel, and A. Vishwanath, Filling-Enforced Gaplessness in Band Structures of the 230 Space Groups, Phys. Rev. Lett. **117**, 096404 (2016).

[54] R. Chen, H. C. Po, J. B. Neaton, and A. Vishwanath, Topological materials discovery using electron filling constraints, Nat. Phys. **14**, 55 (2018).

[55] H. Watanabe, H. C. Po, and A. Vishwanath, Structure and topology of band structures in the 1651 magnetic space groups, Sci. Adv. **4**, eaat8685 (2018).

[56] P. Schobinger-Papamantellos, J. Rodrıguez-Carvajal, G. André, N. P. Duong, K. H. J. Buschow, and P. Tolédano, Simultaneous structural and magnetic transitions in YFe_4Ge_2 studied by neutron diffraction and magnetic measurements, J. Magn. Magn. Mater. **236**, 14 (2001).

[57] G. Kresse and J. Furthmüller, Efficiency of ab-initio total energy calculations for metals and semiconductors using a plane-wave basis set, Comput. Mater. Sci. **6**, 15 (1996).

[58] G. Kresse and J. Furthmüller, Efficient iterative schemes for *ab initio* total-energy calculations using a plane-wave basis set, Phys. Rev. B **54**, 11169 (1996).

[59] G. Kresse and D. Joubert, From ultrasoft pseudopotentials to the projector augmented-wave method, Phys. Rev. B **59**, 1758 (1999).

[60] J. P. Perdew, K. Burke, and M. Ernzerhof, Generalized Gradient Approximation Made Simple, Phys. Rev. Lett. **77**, 3865 (1996).

[61] D. D. Koelling and B. N. Harmon, A technique for relativistic spin-polarised calculations, J. Phys. C **10**, 3107 (1977).

[62] V. I. Anisimov, F. Aryasetiawan, and A. I. Lichtenstein, First-principles calculations of the electronic structure and spectra of strongly correlated systems: the LDA+U method, J. Phys. Condens. Matter **9**, 767 (1997).

[63] Ya. P. Yarmoluk, L. A. Lysenko, and E. I. Gladyshevski, Zirconium iron silicide ($ZrFe_4Si_2$) structure as a new structural type of ternary transition metal silicides, Dopov. Akad. Nauk Ukr. RSR, Ser. A **37**, 279 (1975).

[64] N. V. Belov, N. N. Neronova, and T. S. Smirnova, Shubnikov groups, Sov. Phys. Crystallogr. **2**, 311 (1957).

[65] P. Schobinger-Papamantellos, K. H. J. Buschow, and J. Rodríguez-Carvajal, Magnetoelastic phase transitions in the $LuFe_4Ge_2$ and YFe_4Si_2 compounds: A neutron diffraction study, J. Magn. Magn. Mater. **324**, 3709 (2012).

[66] X. Feng, Electronic structure of MnO and CoO from the B3LYP hybrid density functional method, Phys. Rev. B **69**, 155107 (2004).

[67] F. Ma, W. Ji, J. Hu, Z.-Y. Lu, and T. Xiang, First-Principles Calculations of the Electronic Structure of Tetragonal α-FeTe and α-FeSe Crystals: Evidence for a Bicollinear Antiferromagnetic Order, Phys. Rev. Lett. **102**, 177003 (2009).

[68] H. C. Kandpal, G. H. Fecher, and C. Felser, Calculated electronic and magnetic properties of the half-metallic, transition metal based Heusler compounds, J. Phys. D **40**, 1507 (2007).

[69] B. Balke, G. H. Fecher, H. C. Kandpal, C. Felser, K. Kobayashi, E. Ikenaga, J.-J. Kim, and S. Ueda, Properties of the quaternary half-metal-type Heusler alloy $Co_2Mn_{1-x}Fe_xSi$, Phys. Rev. B **74**, 104405 (2006).

[70] S. Murakami and S.-I. Kuga, Universal phase diagrams for the quantum spin Hall systems, Phys. Rev. B **78**, 165313 (2008).

[71] E. Krén, G. Kádár, L. Pál, J. Sólyom, and P. Szabó, Magnetic structures and magnetic transformations in ordered Mn_3(Rh, Pt) alloys, Phys. Lett. **20**, 331 (1966).

[72] E. Krén, G. Kádár, L. Pál, and P. Szabó, Investigation of the first-order magnetic transformation in Mn_3Pt, J. Appl. Phys. **38**, 1265 (1967).

[73] E. Krén, G. Kádár, L. Pál, J. Sólyom, P. Szabó, and T. Tarnóczi, Magnetic structures and exchange interactions in the Mn-Pt system, Phys. Rev. **171**, 574 (1968).

[74] Z. Q. Liu, H. Chen, J. M. Wang, J. H. Liu, K. Wang, Z. X. Feng, H. Yan, X. R. Wang, C. B. Jiang, J. M. D. Coey *et al.*, Electrical switching of the topological anomalous Hall effect in a non-collinear antiferromagnet above room temperature, Nat. Electron. **1**, 172 (2018).

[75] F. Fei, X. Bo, R. Wang, B. Wu, J. Jiang, D. Fu, M. Gao, H. Zheng, Y. Chen, X. Wang, H. Bu, F. Song, X. Wan, B. Wang, and G. Wang, Nontrivial Berry phase and type-II Dirac transport in the layered material $PdTe_2$, Phys. Rev. B **96**, 041201(R) (2017).

[76] H.-J. Noh, J. Jeong, E.-J. Cho, K. Kim, B. I. Min, and B.-G. Park, Experimental Realization of Type-II Dirac Fermions in a $PdTe_2$ Superconductor, Phys. Rev. Lett. **119**, 016401 (2017).

[77] M. Yan, H. Huang, K. Zhang, E. Wang, W. Yao, K. Deng, G. Wan, H. Zhang, M. Arita, H. Yang *et al.*, Lorentz-violating type-II Dirac fermions in transition metal dichalcogenide $PtTe_2$, Nat. Commun. **8**, 257 (2017).

[78] D. Takane, Z. Wang, S. Souma, K. Nakayama, T. Nakamura, H. Oinuma, Y. Nakata, H. Iwasawa, C. Cacho, T. Kim *et al.*, Observation of Chiral Fermions with a Large Topological Charge and Associated Fermi-Arc Surface States in CoSi, Phys. Rev. Lett. **122**, 076402 (2019).

[79] Q. Wang, Y. Xu, R. Lou, Z. Liu, M. Li, Y. Huang, D. Shen, H. Weng, S. Wang, and H. Lei, Large intrinsic anomalous Hall effect in half-metallic ferromagnet $Co_3Sn_2S_2$ with magnetic Weyl fermions, Nat. Commun. **9**, 3681 (2018).

[80] Y. Wang, E. Liu, H. Liu, Y. Pan, L. Zhang, J. Zeng, Y. Fu, M. Wang, K. Xu, Z. Huang *et al.*, Gate-tunable negative longitudinal magnetoresistance in the predicted type-II Weyl semimetal WTe_2, Nat. Commun. **7**, 13142 (2016).